Article

Influence of Artificial Aging Time on Microstructures and Mechanical Properties of Porthole Die Extruded 6063 Aluminum Alloy

Shikang Li [1,2,*], Fangyu Shen [2], Yu Guo [1,2], Haijun Liu [2] and Changbai Yu [2]

[1] Huzhou Key Laboratory of Green Energy Materials and Battery Cascade Utilization, Huzhou College, Huzhou 313000, China; guoyu@zjhzu.edu.cn
[2] School of Intelligent Manufacturing, Huzhou College, Huzhou 313000, China; liuhaijun@zjhzu.edu.cn (H.L.); yuchangbai@zjhzu.edu.cn (C.Y.)
* Correspondence: lishikang@zjhzu.edu.cn; Tel.: +86-158-6829-8592

Abstract: The influence of artificial aging time on the microstructures and mechanical properties of the 6063 aluminum alloy profile extruded by porthole die was investigated through hardness testing, expansion testing, scanning electron microscope (SEM), and transmission electron microscope (TEM). The results showed that the artificial aging time had a significant impact on the size, morphology, distribution of precipitated phases, and mechanical properties of the porthole die extruded 6063 aluminum alloy profiles. As the artificial aging time increased, the second phase particles gradually precipitated, and the precipitation strengthening gradually enhanced, resulting in an increase in the hardness of the profile. The hardness of the welding zone was lower than that of the matrix zone. Compared with the precipitation in the matrix zone, the size and distribution of the precipitates were uneven, and the time for the precipitation was long in the welding zone due to the influence of grain size. The width of the precipitate free zone (PFZ) in the welding zone was greater than that in the matrix zone. The expansion ratio decreased with the increase of aging time, which indicated that the artificial aging treatment was adverse to the plastic deformation ability of the profiles.

Keywords: aluminum alloy; artificial aging; hardness; welding zone

1. Introduction

The 6xxx series aluminum alloy has been widely used due to its medium strength, high corrosion resistance, and good formability. It is the alloy system with the highest usage among aluminum alloys [1]. The 6xxx series aluminum alloys are often processed into hollow aluminum alloy profiles, which, as typical lightweight components, are widely used in the fields of rail transits, vehicles, ships, building structures, and aerospace. The pothole die extrusion is the key technology to manufacture hollow aluminum alloy profiles. In this process, welding seams are generated [2–4]. Therefore, the control of the microstructure and mechanical properties of the welding zone has become one of the key scientific issues in manufacturing hollow aluminum alloy profiles with high-performance, large-sized, and complex cross-sections.

The mechanical properties of aluminum alloys can be improved in various ways. Zykova et al. [5] achieved an enhancement of the mechanical properties by adding 0.1 mass % of W in Al-Si alloys. Ding et al. [6] conducted heat treatment on Al-20Si powder before extrusion. The eutectic silicon was eliminated and the formability and thermal properties of the Al-20Si alloy were improved. Aluminum alloy is a heat-treatable strengthening alloy, which can achieve good comprehensive mechanical properties through heat treatment [7]. At present, a lot of research about the heat treatment process of 6xxx series aluminum alloys and their impact on the microstructure and mechanical properties has been carried out. Lei et al. [8] analyzed the lattice characterization of precipitates and the grain boundaries of

6013 aluminum in continuous aging. Rymer et al. [9] investigated the influence of artificial aging time on the precipitation characteristics and crack propagation behaviors of 6060 aluminum alloy. Li et al. [10] showed that artificial aging temperatures significantly influenced the precipitation characteristics and corrosion behaviors of the extruded 6082 aluminum alloy. Liu et al. [11] reported that when the new type of 6005A aluminum alloys were subjected to the underage state, their resistance against fatigue crack growths showed the optimum. Engler [12] analyzed the flow stress, work hardening, and plastic anisotropy of 6016 aluminum alloy under various aging treatments. Chae et al. [13] adopted asymmetric rolling and pre/post-aging treatment to improve the mechanical properties and textures of 6061 aluminum alloy. Yang et al. [14] found that aging time had a significant impact on the anti-corrosion resistance of the 6061-T6 aluminum alloy due to the content of the β'' phase. Winter et al. [15] reported that pre-aging enhanced the effect of artificial aging on the hardness and strength of the 6056 aluminum alloy.

In conclusion, aging treatment has a significant impact on the microstructures and mechanical properties of 6xxx series aluminum alloy. However, the research on the effect of aging treatment on the microstructures and mechanical properties of aluminum alloy profiles extruded by porthole die was little and incomplete, especially in the welding zone. LOUKUS et al. [16] studied the microstructures and mechanical properties of AA6082-T4 aluminum alloy during heat treatments and found that Mg_2Si precipitates precipitated along a certain orientation at the transverse weld. Chen et al. [4] studied the evolution of the second phase distribution, grain morphology, size, and texture at the longitudinal weld of an Al-Zn-Mg alloy with different solution times. Xu et al. [3,17,18] found that abnormal grain growth in the weld seam of Al-Li aluminum alloy led to precipitated phases coarsening, precipitating, PFZ widening, and a sharp decrease of elongation during aging.

However, the effect of aging treatment on the 6063 aluminum alloy profile extruded by porthole die extrusion has not been reported yet. As mentioned above, longitudinal welds are inevitably formed during the extrusion process of the porthole die. In addition, compared to other zones, the materials in the welding zones experienced large strains and high pressures. Therefore, compared to other zones, the welded zones usually exhibit a different structure. Aging treatment could improve the microstructure of profiles, especially in the welding zone. Up to now, the evolution of internal microstructure in the welding zone during aging treatment is still unclear.

In this study, porthole die extruded 6063 aluminum alloy hollow profiles were carried out with different extrusion speeds. These profiles containing longitudinal weld seams were subjected to aging treatments at 180 °C at different times. Moreover, the mechanical properties, microstructures, and fracture behaviors of the profiles were characterized and analyzed through hardness testing, expansion testing, SEM, and TEM.

2. Materials and Methods

A 6063 aluminum alloy billet (height 280 mm, diameter 90 mm) was used in this study. The chemical composition of 6063 aluminum alloy billet is shown in Table 1. Firstly, the billets were subjected to homogenization at the temperature of 540 °C for 24 h in a box-type resistance furnace and then cooled to room temperature in the air. Secondly, the homogenized billet was extruded on an 800 t metal profile extruder (Wu Xi Yuanchang Machinery Co., Ltd., Wuxi, China), and the extruded profiles were cooled through online water quenching to achieve a solid solution. In this work, four representative porthole die extrusion experiments were selected, as shown in Table 2. Three extrusion tests were repeated with the same parameters. The inside cross-sectional dimension of the profile was 35 × 35 mm, and the wall thickness was 2.5 mm, as shown in Figure 1. Finally, 6063 aluminum alloy extrusion profiles were immediately subjected to artificial aging treatments with the time of 0.5 h, 1 h, 2 h, 4 h, 6 h, and 8 h at the temperature of 180 °C, respectively, and cooled to room temperature in the air.

Table 1. Chemical composition of 6063 aluminum alloy (wt, %).

Mg	Si	Fe	Cu	Mn	Cr	Zn	Ti	Al
0.85	0.47	0.20	0.21	0.01	0.13	0.25	0.15	Bal

Table 2. Extrusion parameters in this work.

Process Parameters	PE3	PE7	PE9	PE11
Extrusion ratio	16.9	16.9	16.9	16.9
Ram speed (mm/s)	3	7	9	11
Billet temperature (°C)	480	480	480	480
Die temperature (°C)	450	450	450	450
Container temperature (°C)	480	480	480	480
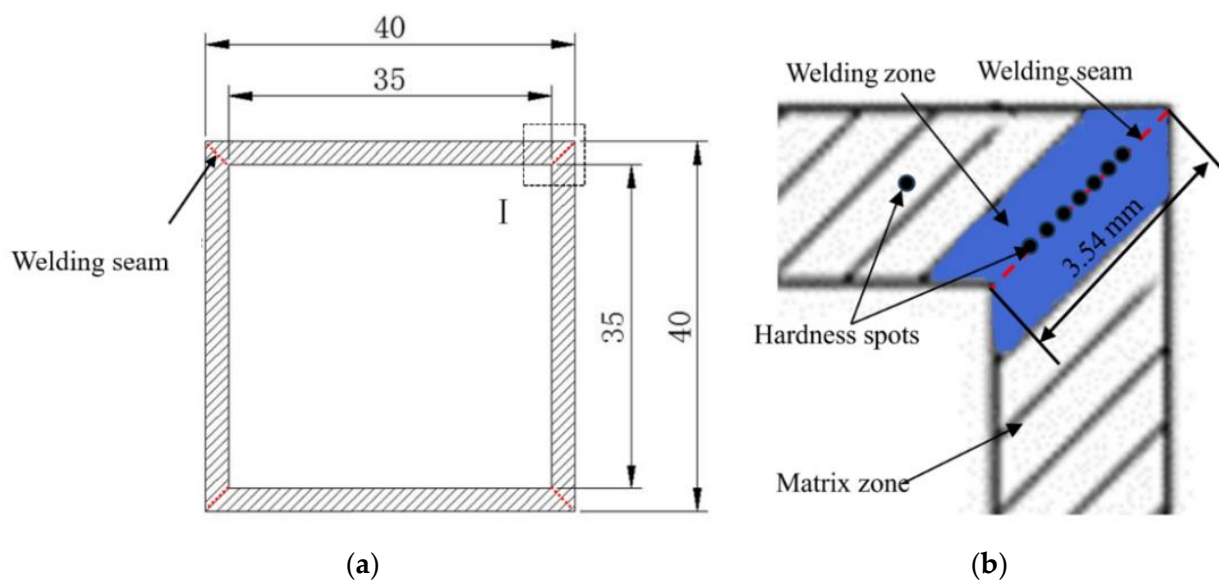
Figure 1. (**a**) Cross-section view of profile and (**b**) close-up view of zone I for microstructure observation and hardness tests.

The hardness of the profiles under different heat treatment conditions was conducted on an HVS-1000 digital microhardness tester (Cany Precision Instruments Co., Ltd., Shanghai, China) with a load of 0.5 kg and a holding time of 15 s. Seven spots from each position were tested for hardness, as shown in Figure 1. The maximum and minimum values were removed and the average of the remaining five hardness values was the final result. The samples for TEM observations were ground to a thickness of 80 μm and then prepared using an ion milling machine with a Struers Tenupol-5 (Struers, Aarhus, Denmark). The TEM observations were performed using a Tecnai G2 F20 S-TWIN (Frequency Electronics, Inc., New York, NY, USA) microscope operating with an acceleration voltage of 200 kV.

The quality of the longitudinal welding seam of the hollow profile can be estimated through an expanding test using a conical punch, as shown in Figure 2. The strength of the welding seam is quantified by the expansion ratio [19–21]. The expanding ratio is defined as $\alpha = d_m / d_0$, where d_m is the equivalent diameter of the inner area of the extruded square tube before fracture and d_0 is the equivalent diameter of the inner area of the extruded square tube. The expanding test was conducted on the INSTRON3369 electronic universal material testing machine (INSTRON CORPORATION, Norwood, MA, USA). The pressing speed was set as 2 mm/min. The fracture morphologies of expanding samples were observed by SEM with an FEI QUANTA 200 (Frequency Electronics, Inc., New York, NY, USA).
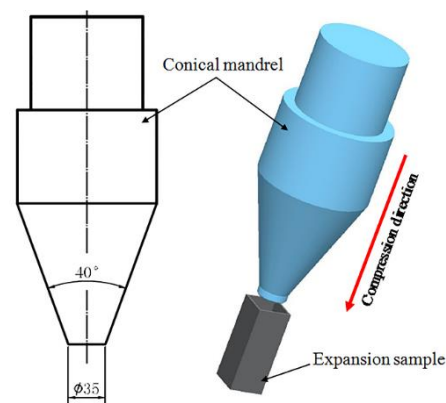
Figure 2. Expanding test for extruded tubes.

3. Results and Discussion

3.1. Microstructure and Hardness

Figure 3 gives the optical microstructure of the cross-sections of PE3, PE7, PE9, and PE11. For the profile of PE3 and PE7, there was a welding zone in the central zones, as shown in Figure 3a,b. For the profile of PE9, there was only a welding seam in the central zone, as shown in Figure 3c. The welding zone gradually narrowed down and finally disappeared, as shown in Figure 3d. There was no obvious feature in the central zone of PE11. Optical observations indicated that the weld seams had the most obvious characteristics in the central zones on the cross-section of the porthole die extrusion profiles in this study. The average grain sizes of extrudate profiles were measured using the ASTM-E1382 linear intercept length method in two evenly spaced directions (0° and 90°). Table 3 displays the average grain sizes of extrudate profiles. At the ram speed of 3 mm/s, 7 mm/s, 9 mm/s, and 11 mm/s, the grain size in the welding zone was 86 μm, 49 μm, 52 μm, and 54 μm, respectively. While, in the matrix zone, the grain size was 49 μm, 34 μm, 37 μm, and 39 μm, respectively.
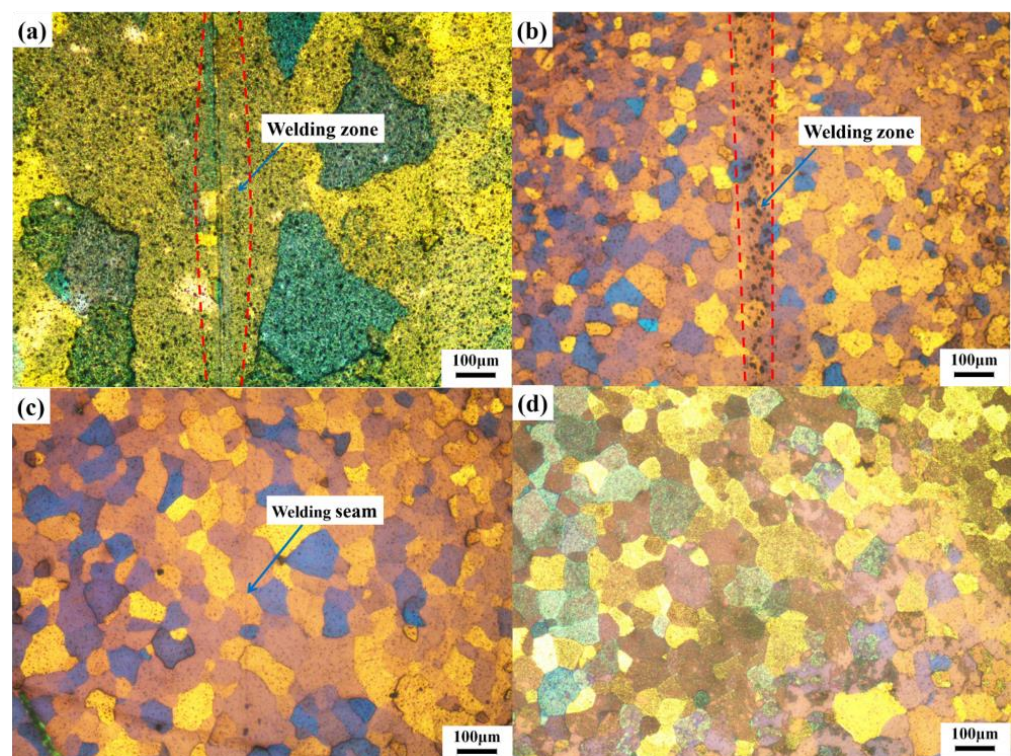

Figure 3. Microstructure and welding zones of (**a**) PE3, (**b**) PE7, (**c**) PE9, and (**d**) PE11.

Table 3. Average grain sizes of extrudate profiles. (Unite: μm).

Zone	Ram Speed (mm/s)			
	3	7	9	11
Welding zone	86	49	52	54
Matrix zone	49	34	37	39

Figure 4 shows the effect of aging time on the hardness of the 6063 aluminum alloy profile. As the aging time and ram speed increased, the hardness first increased and then remained stable. The peak aging time in the matrix zone was shorter than that in the welding zone. This was because the grain size of the extruded profile in the matrix zone is generally lower than that in the welding zone in this study [22], leading to an enhanced yield strength [23,24] and precipitation strengthening [25–27]. Figure 4a presents the changes in the hardness of the profile extruded at the ram speed of PE3 with respect to the aging time. There was always a difference in hardness between the matrix zone and the welding zone of PE3 and PE7, and the hardness of PE3 was significantly lower than those of PE7, PE9, and PE11, as shown in Figure 4b–d. That was due to the low solid solubility caused by the low ram speed, especially in the welding zone. Moreover, as the ram speed and aging time increased, the difference in hardness between the welding zone and the matrix zone gradually decreased and finally became equal.
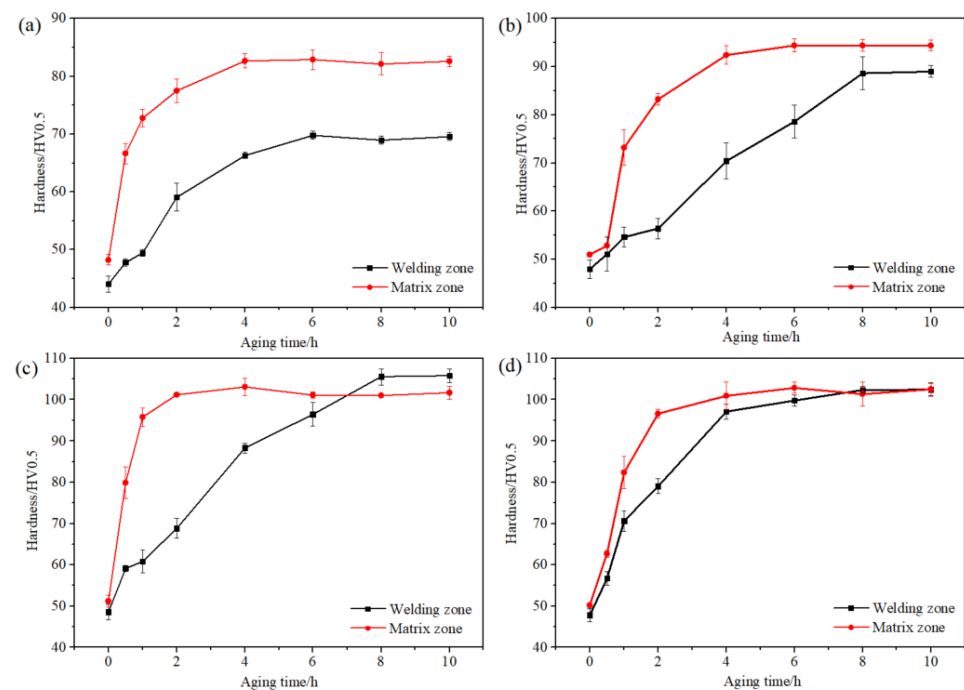
Figure 4. Influence of aging time on the hardness of (**a**) PE3, (**b**) PE7, (**c**) PE9, and (**d**) PE11.

3.2. Microstructure

Figure 5 shows the TEM observation images of PE3 without artificial aging treatment. Figure 5a shows that no obvious precipitates in the TEM image in the matrix zone. From the electron diffraction image, it can be seen that there were only diffraction spots of aluminum, which indicated that there were no precipitates in the matrix zone of the extruded profile without artificial aging treatment. There were some dislocations in the welding zone, and no obvious precipitates were observed in Figure 5b. The above experimental phenomenon indicated that the profile of PE3 was in a supersaturated state. The same phenomenon was also observed in the profiles of PE7, PE9, and PE11.
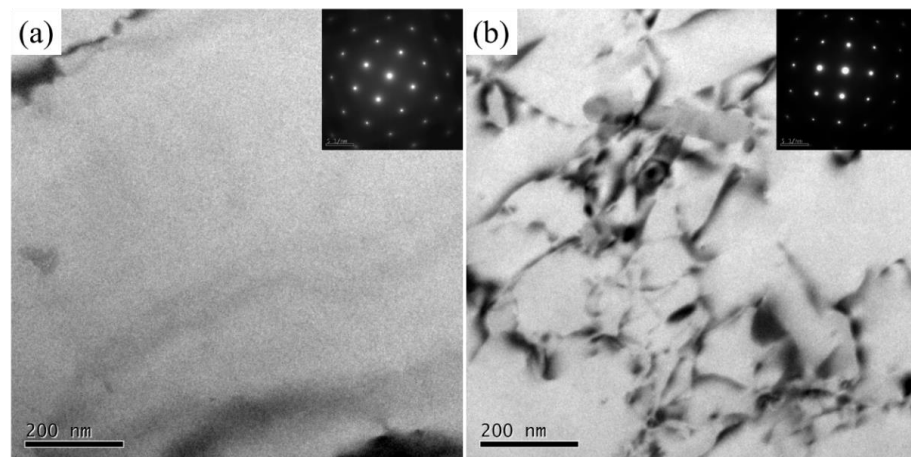
Figure 5. TEM morphology in (**a**) the matrix zone and (**b**) welding zone of PE3 without artificial aging treatment.

Figure 6 shows the TEM morphology of PE3 when the artificial aging time was 1 h. Figure 6a shows the distribution of precipitates in the matrix zone. A lot of dispersed and fine precipitates were observed. Figure 6b gives the bright field TEM image in the welding zone. There were no obvious precipitates. High-resolution observations were performed in the matrix zone of PE3, as shown in Figure 6c,d. The size and distribution of precipitates were uniform, needle-like precipitates with a length of approximately 12–17 nm and a thickness of approximately 3 nm were observed. According to references [25,26,28], the β″ phase was formed by the GP zone growing along the direction of the matrix [100], with a length of 12–200 nm and a needle-like shape. Therefore, it can be determined that the precipitate was β″ phase in the profile. Compared to the precipitates in the matrix zone, the number of precipitates in the welding zone was small, the size was varied, and the distribution was uneven, which led to the low hardness in the welding zone, as shown in Figure 4.
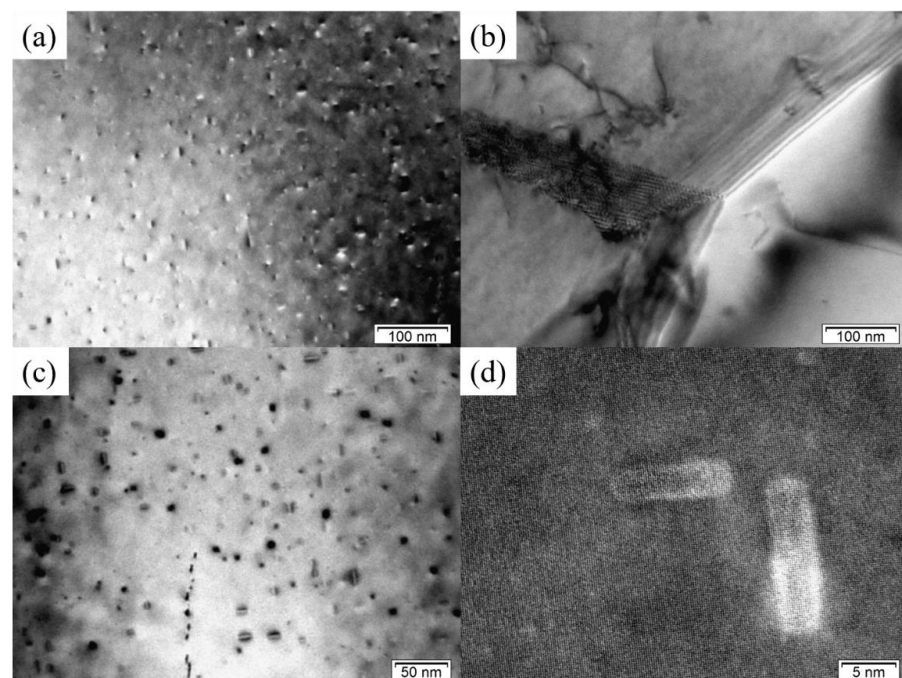

Figure 6. TEM morphology in (**a**) the matrix zone, (**b**) welding zone, and (**c**,**d**) high-resolution image at two magnifications in the matrix zone of PE3 with aging for 1 h.

Figure 7 shows the bright field image of precipitates after 8 h of PE3. A large number of needle-like precipitates were observed. Compared with aging for 2 h, there was no significant increase in the number of precipitates, but there was a significant growth of precipitates in the matrix zone, as shown in Figure 7a. The number of needle-like precipitates in the welding zone significantly increases, and there is growth in the length direction of the precipitates, as shown in Figure 7b. The distribution of precipitates in the welding zone is more uneven than that in the matrix zone.
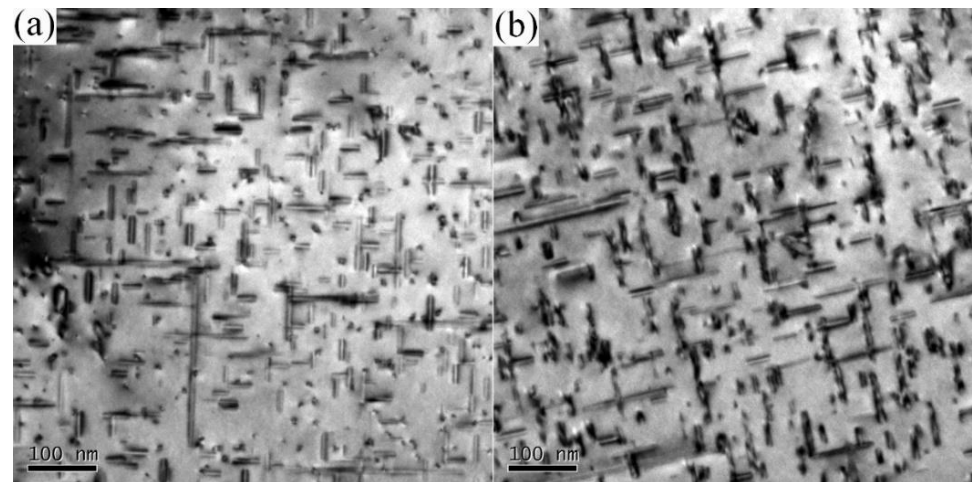

Figure 7. TEM morphology in (**a**) the matrix zone and (**b**) welding zone of PE3 with aging for 8 h.

Figure 8 shows the TEM image in the PE9 when the aging time was 1 h. A large number of dispersed and fine precipitates were observed in the matrix zone, with a length of approximately 23 nm, as shown in Figure 8a. There was no obvious precipitation phase in the welding zone, as shown in Figure 8b, which indicated that the internal structure of the profile had a certain impact on the aging precipitation behavior, resulting in different mechanical properties, as shown in Figure 4. Figure 9 shows the TEM image in the PE9 when the aging time was 8 h. A large number of needle-like precipitates were observed. The distribution of these needle-like precipitates was uniform. The length of the precipitates was about 40–50 nm. There was no significant difference between the precipitates in the matrix zone and the welding zone, which was consistent with the hardness results in Figure 4. Compared to the precipitation of PE9 aging for 1 h, the number of needle-like precipitates was much more, and the size and distribution were more uniform with aging for 8 h.
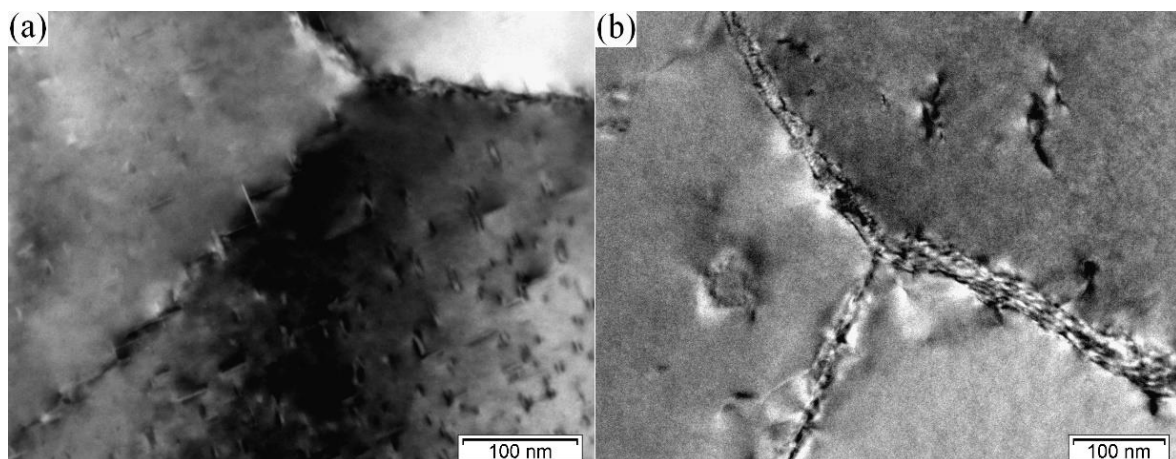

Figure 8. TEM morphology in (**a**) the matrix zone and (**b**) welding zone of PE9 with aging for 1 h.
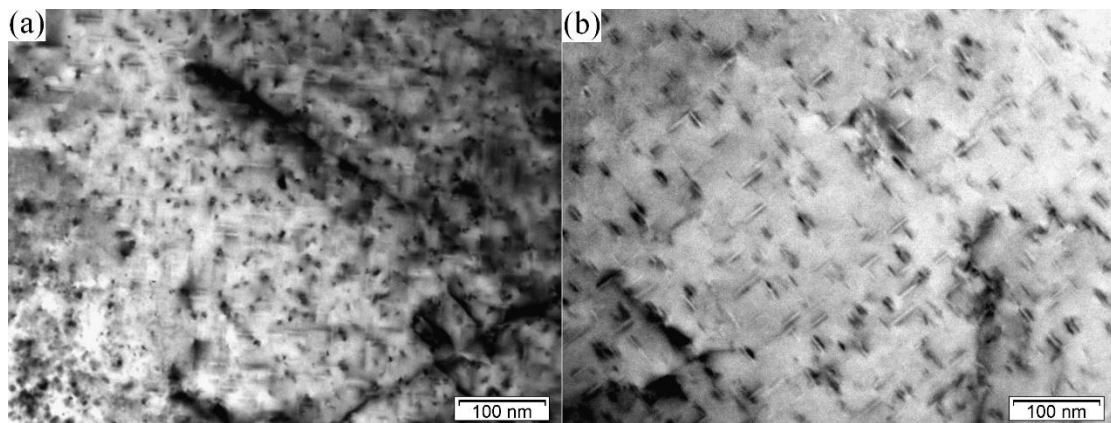
Figure 9. TEM morphology in (**a**) the matrix zone and (**b**) welding zone of PE9 with aging for 8 h.

A saturated solid solution would be formed in the profile during the online quenching process, as shown in Figure 5. The solid solution atoms of Mg and Si were in a metastable state and would precipitate in a certain sequence in the artificial aging process [28–30]. Firstly, Si and Mg atoms were clustered, respectively, and then Mg atoms, or the decomposed Mg atoms, moved towards the Si atom clusters to form Mg/Si atom clusters, which was known as the G.P. zone. The G.P. zone formed in the early stage of artificial aging maintained a coherent relationship with the parent phase, which had an internal strain-strengthening effect and increased the hardness of the profile, as shown in Figure 4. The G.P. zone was in a thermodynamic metastable state. As the G.P. zone grew and transformed into the β'' phase, the G.P. zone gradually disappeared. At this time, the G.P. zone and β'' phase coexisted, as shown in Figure 10. In the early stage, the size of the β'' phase was relatively small and dislocation could cut through it. When dislocations forcibly passed through the β'' phase, they needed to overcome the stress field. The surface energy was increased when the β'' phase was cut into two parts, resulting in a further increase in strength. The β'' phase gradually grew with the increase of aging time, as shown in Figure 9, and its hindrance to the movement of dislocation increased, resulting in an increase in the mechanical properties of profiles.
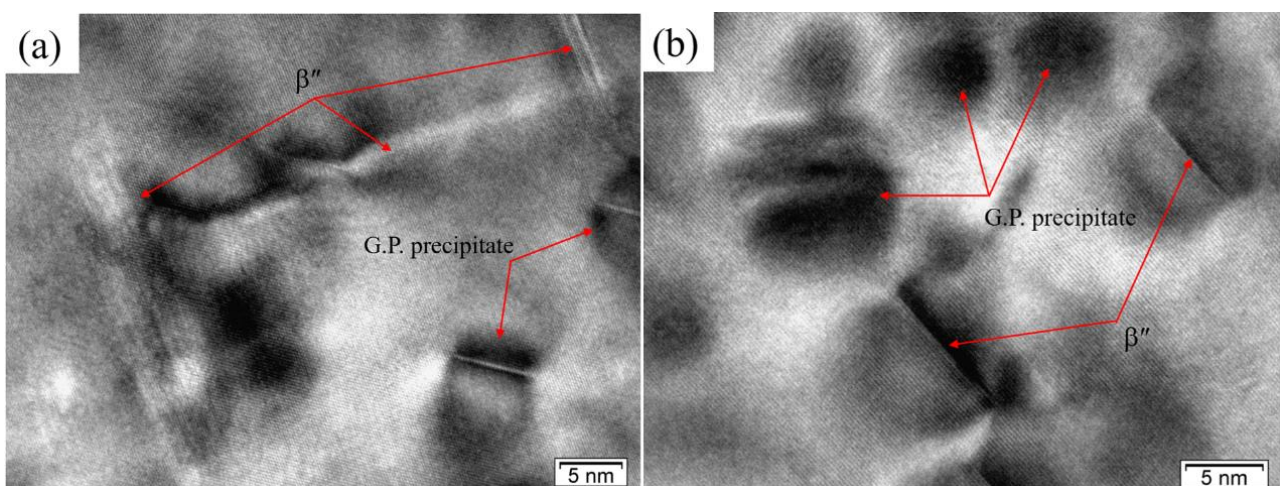

Figure 10. TEM morphology in (**a**) the matrix zone and (**b**) welding zone of PE7 with aging for 1 h.

According to references [25–27], the precipitation rate and precipitation zone were greatly affected by the internal structure of the alloy. The research results of Chrominski et al. [25,26] and Quispe et al. [27] indicated that fine grains were beneficial for shortening the peak aging time. The incubation period and growth time required for precipitates was

long in the large grain size. The grain size of the extruded profile in the matrix zone is generally lower than that in the welding zone in this study [22,31]. Therefore, during the artificial aging process, the incubation period required for the precipitates was shorter and the precipitation was more complete in the matrix zone, as shown in Figures 6–8.

Figure 11 shows the TEM images of PFZ in the PE3 when the aging time was 2 h. There were a large number of precipitates in the grains, and PFZs were observed along the grain boundaries, as shown by the red dashed lines. The size and distribution of precipitates in the matrix zone were more uniform than those in the welding zone. The width of PFZ with aging time is shown in Table 4. It can be seen that: (1) The width of PFZ firstly increased and then decreased with the increase of aging time. This was because as the aging time increased, the precipitates in the profile gradually grew, and the precipitates near the grain boundaries extended towards the grain boundaries, resulting in a short width of the PFZ. (2) As the extrusion speed increased, the width of PFZ gradually decreased. This was due to the high extrusion speed leading to the short time for the profile from the mold outlet to the water during extrusion. There was no time for vacancy migration, resulting in a decrease in vacancy concentration along the grain boundary and the narrow width of PFZ. (3) The width of PFZ in the welding zone was greater than that in the matrix zone, which was due to the low temperature in the welding zone of the extruded profile.
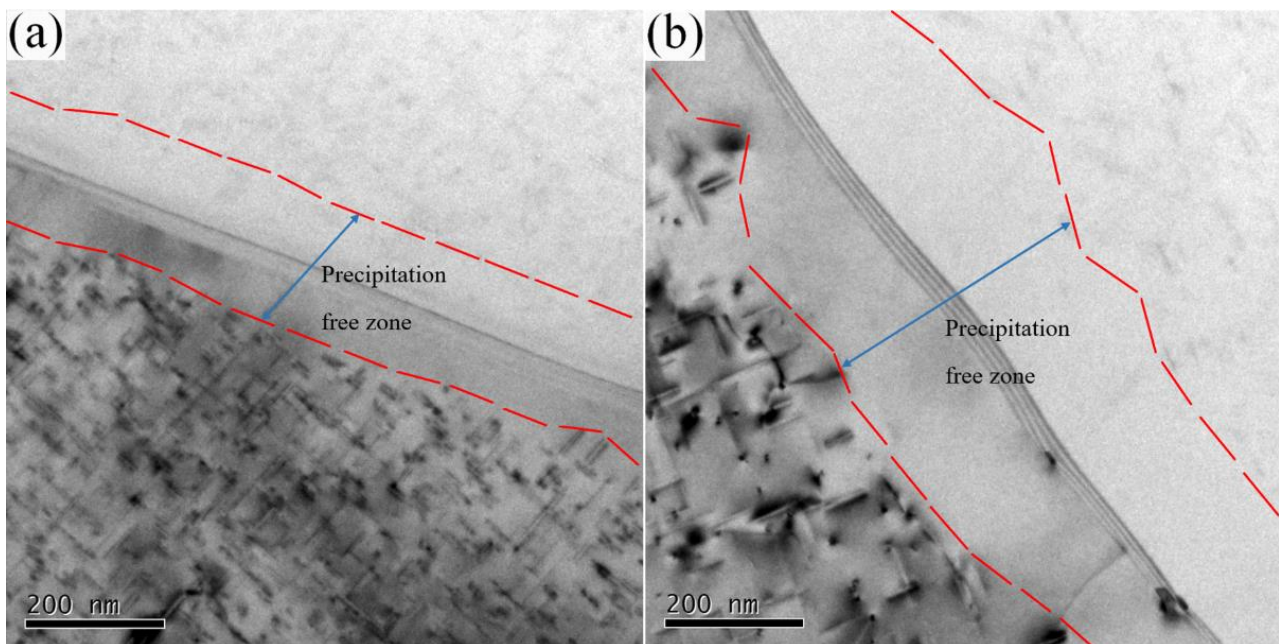

Figure 11. TEM morphology of PFZ in (**a**) the matrix zone and (**b**) welding zone of PE3 with aging for 2 h.

Table 4. The width of PFZ with different aging times (M and W represented the matrix zone and welding zone, respectively).

Aging Time (h)	Width of PFZ (nm)							
	3 mm/s		7 mm/s		9 mm/s		11 mm/s	
	W	M	W	M	W	M	W	M
1	261	187	201	127	159	143	132	78
2	421	210	289	145	267	123	143	110
4	422	234	301	189	257	172	178	165
8	316	295	302	268	230	190	175	156

Plastic deformation was easily concentrated within the PFZ due to its low yield strength, leading to intergranular fracture. Therefore, most researchers believed that PFZ was harmful. STARINK et al. [32] found that the formation of PFZ caused a sharp decrease in the alloy strength of 100 MPa, but it did not affect the peak aging time. Krol et al. [33] found that when the width of PFZ reached 440 nm, the yield strengthening of the alloy decreased by 22%. MUNITZ et al. [34,35] discussed the relationship between PFZ and fracture morphology and found that the narrower the PFZ, the higher the mechanical properties of the alloy. The PFZ would affect the morphology of the dimple.

3.3. Mechanical Properties

3.3.1. Expansion Test

The fracture surface of the profile after the expansion test is shown in Figure 12. All cracks initiated at the corners of the square tube and propagated during expansion. The crack propagation distances along the weld seam under different aging times are shown in Figure 13. It can be seen that as the aging time increased, the propagation distance of cracks along the weld seam gradually increased. It can be seen that the propagation distance of the crack along the weld seam after 4 h of aging was very close to the theoretical length of the weld seam of 3.54 mm, as shown in Figure 1, indicating that cracks completely propagated along the welding seam during the expansion process. Moreover, the propagation distance of the crack along the weld seam slowly increased with the increase of ram speed and then decreased before aging for 4 h. That may be due to the dual effects of recrystallization and welding strength in the welding zone.

Figure 12. Macro-morphology of fracture after expanding test of PE11 with an aging time of (**a**) 2 h and (**b**) 8 h.
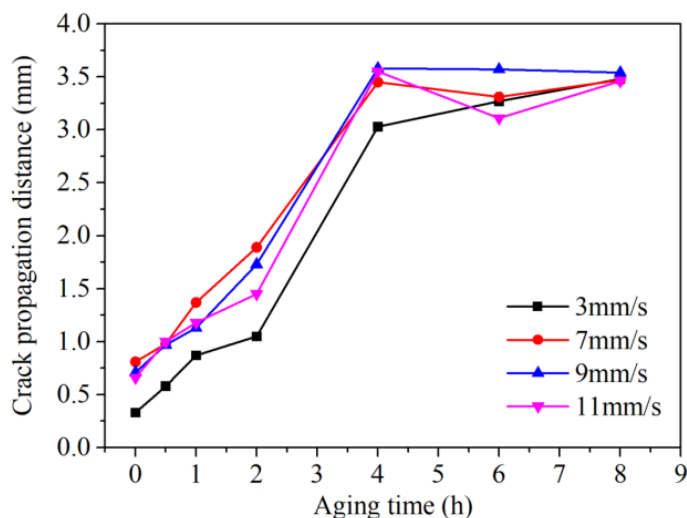
Figure 13. Crack propagation distance along the weld seam with artificial aging treatment.

Further observation of Figure 12 shows that the fracture surface of the profile underwent significant plastic deformation. This fracture was not a dangerous brittle fracture, and the profile had a certain damage tolerance, indicating that the 6063 aluminum alloys had been fully welded during the extrusion process. From the expansion pressure-displacement curve (Figure 14), it can be seen that as the aging time increased, the ability of the profile to withstand lateral forces gradually decreased. The expansion ratios of PE3, PE7, PE9, and PE11 decreased from 1.25, 1.15, 1.17, and 1.20 to 1.06, 1.05, 1.04, and 1.06, respectively, as shown in Figure 15. The maximum reduction was 15.4%. The decreasing trend with increasing aging time indicated that aging heat treatment weakened the plastic deformation ability of the profile.
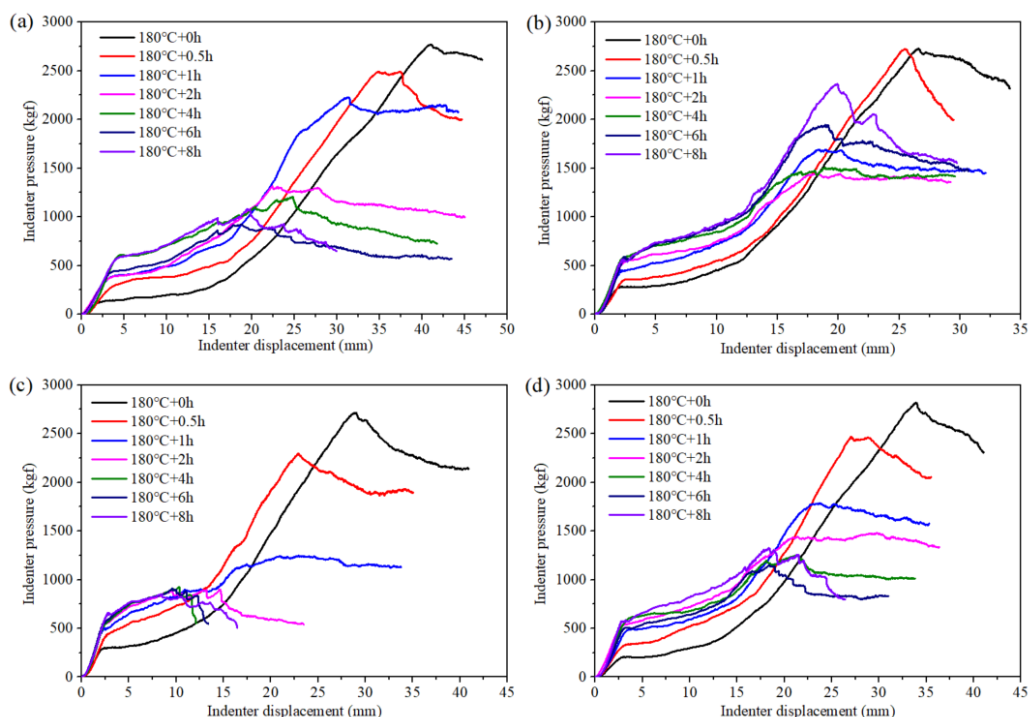

Figure 14. Pressure-displacement curves during expansion tests of (**a**) PE3, (**b**) PE7, (**c**) PE9, and (**d**) PE11.
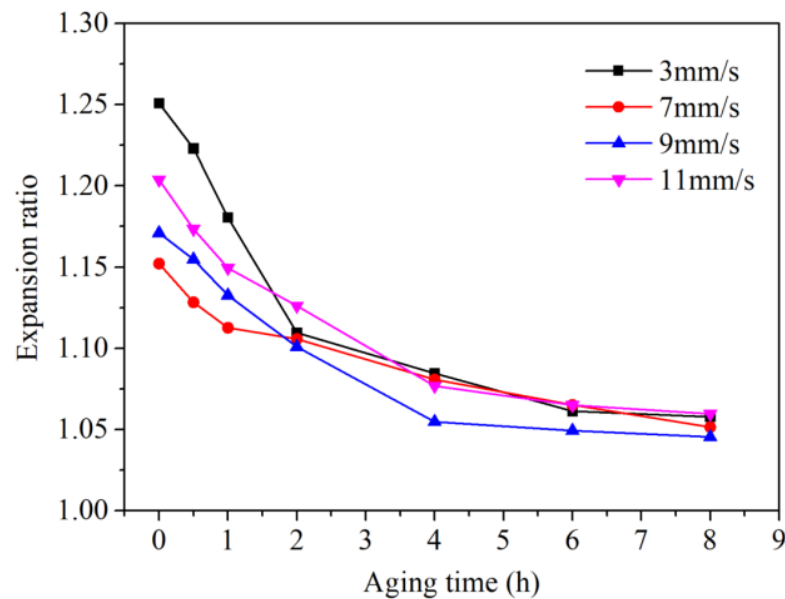
Figure 15. Expansion ratio-aging time curves of 6063 aluminum alloy profile.

According to references [36–38], as time increased, the precipitates gradually precipitated and grew, and the yield strength and tensile strength of aluminum alloys gradually increased. However, the uniform elongation, the total elongation, and the strain hardening factor of the aluminum alloy gradually decreased, which was not conducive to expansion testing. Moreover, based on the diffusion mechanisms, there was much time for the movement of the atoms at a low ram speed, resulting in a high welding strength and expansion ratio, as shown in the profile of PE3. Furthermore, according to the study of He et al. [39], homogeneous microstructure was beneficial for improving ductility. During the 6063 aluminum porthole die extrusions, the occurrence of DRX caused a refinement in grain size and uniform microstructure of PE11, and weakened the presence of the welding zone, as shown in Figure 1. Therefore, the expansion ratio increased the increase of ram speed from 7 mm/s to 11 mm/s.

3.3.2. Fractography

The full view of the fracture morphology of PE3 with aging for 4 h after the expansion test is shown in Figure 16. A similar typical cup-and-cone fracture was observed. The fracture surface was flat and had no large tearing planes. Figure 16b,c gives the fracture micro-morphologies of the (b) and (c) zones in Figure 16a, respectively, where a large number of large and deep equiaxed dimples could be observed, exhibiting a fracture characteristic of a typical dimple fracture. Constituent particles were observed at the bottom of the dimples. Some dimples did not contain any particles, but this did not exclude their existence as they might have fallen off or still exist in opposite fracture surfaces. The particles were the nucleation sites of voids due to breakages of particles and/or debonding between particles and the matrix [40]. A large number of particles indicated that the initiation, growth, and aggregation of the void were the main physical mechanisms of fracture in the PE3 with aging for 4 h. The full view of the fracture morphology of PE3 with aging for 8 h after the expansion test is shown in Figure 17. The fracture surface was flatter than that with aging for 4 h. Figure 17b gave the fracture micro-morphologies of the (b) zone in Figure 17a, where the dimples, which indicated intergranular mode and good ductility [40,41], were also observed on the fracture surfaces. Compared with the fracture morphology of PE3 with aging for 4 h, the distribution of the dimples aged for 8 h was more uniform, and the size was larger.
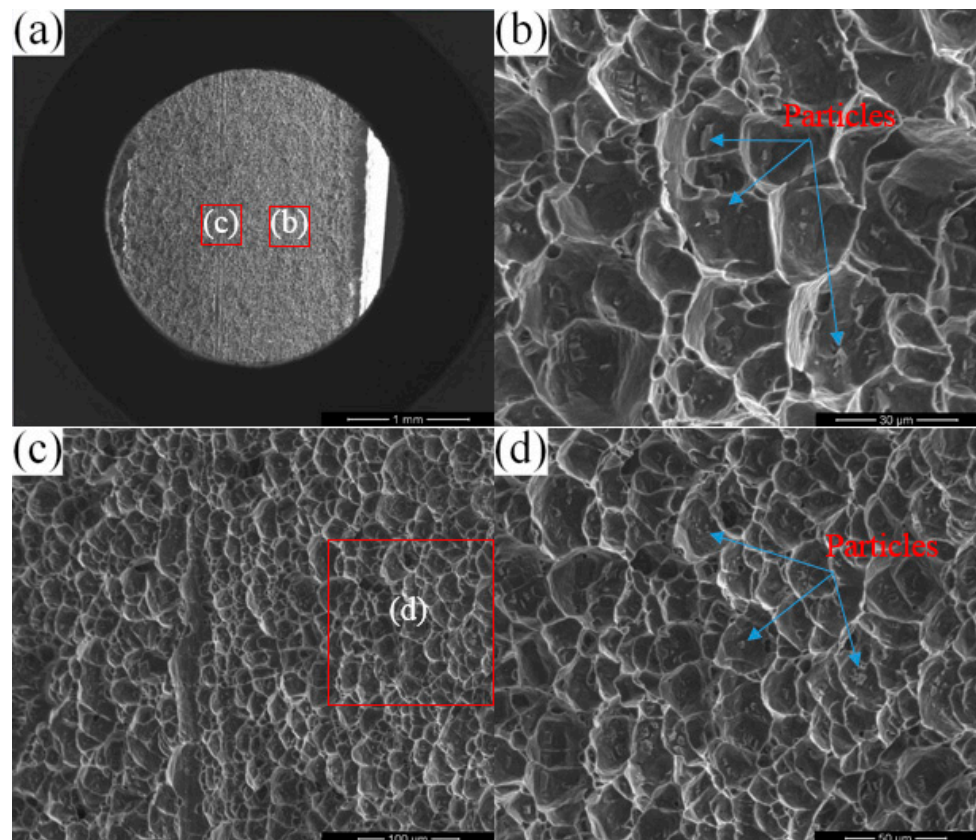
Figure 16. Fracture morphology of PE3 after expansion test with aging for 4 h: (**a**) full view of the fracture morphology, (**b**) close-up view of (**b**) zone in Figure 16a, (**c**) close-up view of (**c**) zone in Figure 16a and (**d**) close-up view of (**d**) zone in Figure 16c.
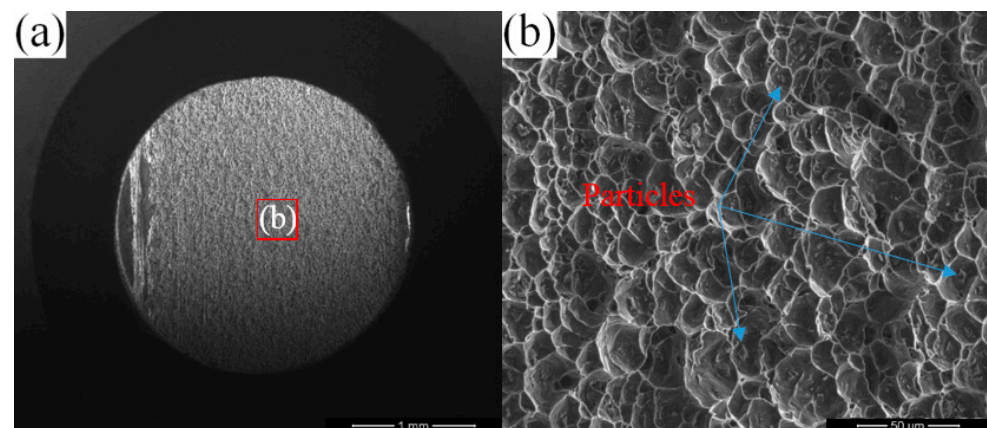

Figure 17. Fracture morphology of PE3 after expansion test with aging for 8 h: (**a**) full view of the fracture morphology, (**b**) close-up view of (**b**) zone in Figure 17a.

The global image of the fracture morphology of PE9 after aging for 4 h is shown in Figure 18a. The fracture surface was not flat and a clear ridge-like morphology in the central region was observed, as shown in Figure 18b. Compared with the fracture morphology of the PE3 aged for 4 h, the fracture morphology of the PE9 sample aged for 4 h was characterized by fewer, smaller, and shallower dimples, which were separated by longitudinal stripes along the extrusion direction, demonstrating the ability to exhibit a poor plastic deformation, which corresponded well with the expansion ratio.
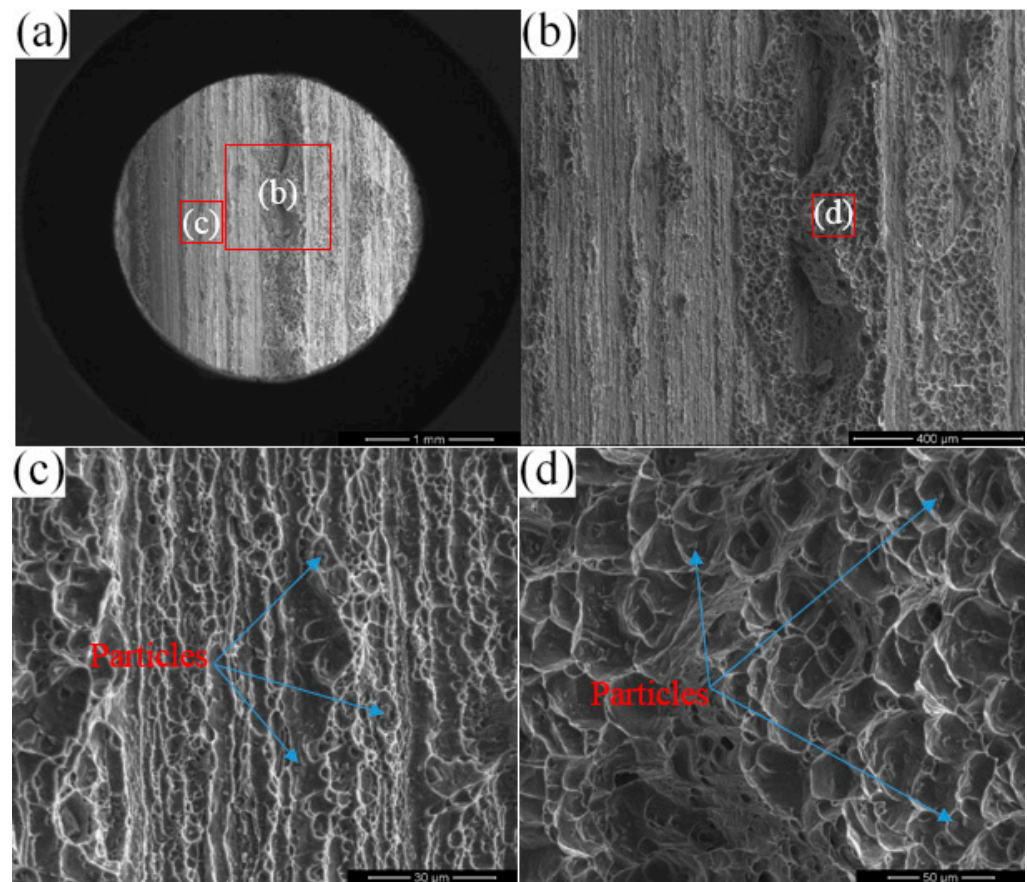
Figure 18. Fracture morphology of PE9 after expansion test with aging for 4 h: (**a**) full view of the fracture morphology, (**b**) close-up view of (**b**) zone in Figure 18a, (**c**) close-up view of (**c**) zone in Figure 18a and (**d**) close-up view of (**d**) zone in Figure 18b.

Due to its good welding performance, the difference in mechanical properties between the matrix zone and the welding zone was low. With the progress of artificial aging, due to the differences in grain sizes between the welding zone and the matrix zone, the morphology, size, distribution, and precipitation rate of precipitates between the welding zone and the matrix zone were different. The precipitation rate of the welding zone with larger grain size was slow, and the mechanical property was lower than that of the matrix zone, as shown in Figures 4, 17 and 18. The large grain size in the welding zone would be negative for the ductility of the profile [42]. During the artificial aging process, the precipitation of Mg/Si atomic clusters and β'' phases in 6000 series aluminum alloys was beneficial for improving the mechanical strength of the material [43,44], as shown in Figure 4. At the same time, it also reduced the ductility of the profile, resulting in a low expansion ratio, as shown in Figure 15. During the expansion, crack propagation exhibited different modes and fracture morphology. Moreover, as the artificial aging time increased, the precipitates gradually grew, and the PFZ was formed at the grain boundary. The yield strength of PFZ was relatively low. During the expansion process, strain was easily concentrated within the precipitated zone under stress, causing the initiation of cracks. Furthermore, as the formation of PFZ happened, coarse and dispersed precipitates were formed at grain boundaries, as shown in Figure 19. The coarse and dispersed precipitates cannot hinder the movement of dislocations, but they reduce the saturation within the grain, resulting in a decrease in the strength and elongation of the profile.
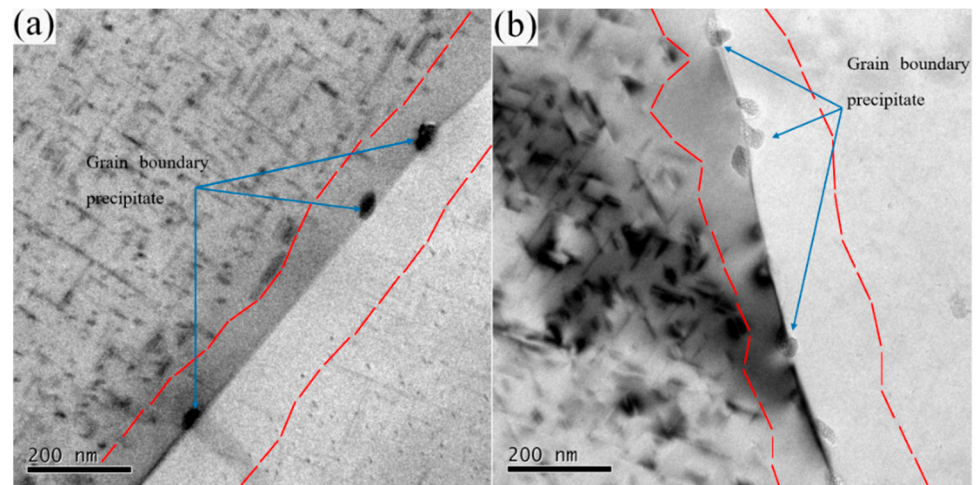
Figure 19. Coarse and dispersed precipitates at the grain boundary in (**a**) the matrix zone and (**b**) welding zone of PE7 with aging for 2 h.

4. Conclusions

In this study, the artificial aging treatment on the porthole die extruded 6063 aluminum alloy profile was conducted at 180 °C at different times. The hardness and expansion testing, TEM observation, and SEM fracture morphology analysis were performed. The microstructures and mechanical properties of the matrix and welding zone under different artificial aging times were studied. Based on the presented results, the following conclusions can be drawn:

(1) With the increase of artificial aging time, the hardness of the 6063 aluminum alloy profile gradually increased due to the precipitation and growth of the β'' phase.

(2) Due to the difference in grain size, the size and distribution of the precipitates were more uneven, and the time for the precipitation was longer in the welding zones than those in the matrix zones. Therefore, the hardness of the welding zone was lower than that of the matrix zone of the 6063 aluminum alloy profile.

(3) As the artificial aging time increased, the expansion ratio of the profile sharply decreased. The maximum reduction was 15.4%. The decreasing trend with increasing aging time indicated that aging heat treatment weakened the plastic deformation ability of the profile.

(4) The results obtained in this study could provide significant theoretical support and basic data for further study in the field of porthole die extrusion.

Author Contributions: Conceptualization, S.L., F.S. and Y.G.; methodology, S.L., F.S., Y.G., H.L. and C.Y.; validation, S.L., F.S. and C.Y.; formal analysis, S.L., Y.G. and C.Y.; investigation, S.L., F.S., Y.G. and C.Y.; writing—original draft preparation, S.L. and F.S.; writing—review and editing, S.L., F.S., Y.G., H.L. and C.Y.; visualization, S.L. and C.Y.; supervision, S.L. and Y.G.; project administration, S.L., Y.G., H.L. and C.Y.; funding acquisition, S.L. and F.S. All authors have read and agreed to the published version of the manuscript.

References

1. Yu, X.; Zhang, G.; Zhang, Z.; Wang, Y. Research on corrosion resistance of anodized and sealed 6061 aluminum alloy in 3.5% sodium chloride solution. *Int. J. Electrochem. Sci.* **2023**, *18*, 100092.
2. Hwang, Y.M.; Hsu, I.P. Die Design and Finite Element Analysis of Welding Seams during Aluminum Alloy Tube Extrusion. *Metals* **2023**, *13*, 911.
3. Xu, X.; Ma, X.; Zhao, G.; Wang, Y.; Chen, X. Effects of abnormal grain growth at longitudinal weld on the aging behavior and mechanical properties of 2196 AlCuLi alloy profile. *Mater. Des.* **2021**, *210*, 110043.
4. Chen, G.; Chen, L.; Zhao, G.; Zhang, C. Microstructure evolution during solution treatment of extruded Al-Zn-Mg profile containing a longitudinal weld seam. *J. Alloys Compd.* **2017**, *729*, 210–221.
5. Ding, C.; Hao, H.; Lu, Z.; Yu, C.; Wu, X.; Yu, P.; Ye, S. Fabrication of hypereutectic Al–Si alloy with improved mechanical and thermal properties by hot extrusion. *Mater. Charact.* **2023**, *202*, 113026.
6. Zykova, A.; Martyushev, N.; Skeeba, V.; Zadkov, D.; Kuzkin, A. Influence of W Addition on Microstructure and Mechanical Properties of Al-12%Si Alloys. *Materials* **2019**, *12*, 981–990.
7. Granum, H.; Myhr, O.R.; Børvik, T.; Hopperstad, O.S. Effect of pre-stretching on the mechanical behaviour of three artificially aged 6xxx series aluminium alloys. *Mater. Today Commun.* **2021**, *27*, 102408.
8. Lei, G.; Wang, B.; Lu, J.; Wang, C.; Li, Y.; Luo, F. Microstructure, mechanical properties, and corrosion resistance of continuous heating aging 6013 aluminum alloy. *J. Mater. Res. Technol.* **2022**, *18*, 370–383.
9. Rymer, L.M.; Winter, L.; Hockauf, K.; Lampke, T. Artificial aging time influencing the crack propagation behavior of the aluminum alloy 6060 processed by equal channel angular pressing. *Mater. Sci. Eng. A* **2021**, *811*, 141039.
10. Yang, L.; Bai, D.; Wang, D.; Liu, C.; Yang, S.; Huang, G. Effect of aging temperature on microstructure and corrosion behavior of 6082 aluminum alloy. *Mater. Today Commun.* **2023**, *36*, 106583.
11. Liu, Y.; Pan, Q.; Liu, B.; Yu, Q.; Li, G.; Pan, D. Effect of aging treatments on fatigue properties of 6005A aluminum alloy containing Sc. *Int. J. Fatigue* **2022**, *163*, 107103.
12. Engler, O. Effect of precipitation state on plastic anisotropy in sheets of the age-hardenable aluminium alloys AA 6016 and AA 7021. *Mater. Sci. Eng. A* **2022**, *830*, 142324.
13. Chae, W.; Jeong, M.; Lee, D.; Lee, J.; Chun, D.W.; Lee, S.Y.; Hong, S.K.; Kim, S.H.; Han, J.H. Effects of pre/post-aging treatment on the mechanical properties and texture of asymmetrically rolled 6061 aluminum alloy: Formability and planar anisotropy. *J. Mater. Res. Technol.* **2023**, *24*, 9476–9490.
14. Yang, J.; Zhao, B.; Zhu, M.; Liu, L.; Zhang, X. Influence of aging time on the corrosion behavior of 6061-T6 aluminum alloy in NaCl solution. *Int. J. Electrochem. Sci.* **2021**, *16*, 211231.
15. Winter, L.; Hockauf, K.; Scholze, M.; Hellmig, R.J.; Lampke, T. Influence of Pre-Aging on the Artificial Aging Behavior of a 6056 Aluminum Alloy after Conventional Extrusion. *Metals* **2021**, *11*, 385.
16. Loukus, A.; Subhash, G.; Imaninejad, M. Mechanical properties and microstructural characterization of extrusion welds in AA6082-T4. *J. Mater. Sci.* **2004**, *39*, 6561–6569. [CrossRef]
17. Xu, X.; Zhao, G.; Yu, S.; Wang, Y.; Chen, X.; Zhang, W. Effects of extrusion parameters and post-heat treatments on microstructures and mechanical properties of extrusion weld seams in 2195 Al-Li alloy profiles. *J. Mater. Res. Technol.* **2020**, *9*, 2662–2678.
18. Xu, X.; Ma, X.; Zhao, G.; Chen, X.; Wang, Y. Abnormal grain growth of 2196 Al-Cu-Li alloy weld seams during extrusion and heat treatment. *J. Alloys Compd.* **2021**, *867*, 159043.
19. Jo, H.H.; Jeong, C.S.; Lee, S.K.; Kim, B.M. Determination of welding pressure in the non-steady-state porthole die extrusion of improved Al7003 hollow section tubes. *J. Mater. Process. Technol.* **2003**, *139*, 428–433. [CrossRef]
20. Kim, K.J.; Lee, C.H.; Yang, D.Y. Investigation into the improvement of welding strength in three-dimensional extrusion of tubes using porthole dies. *J. Mater. Process. Technol.* **2002**, *130–131*, 426–431. [CrossRef]
21. Li, L.; Zhang, H.; Zhou, J.; Duszczyk, J.; Li, G.Y.; Zhong, Z.H. Numerical and experimental study on the extrusion through a porthole die to produce a hollow magnesium profile with longitudinal weld seams. *Mater. Des.* **2008**, *29*, 1190–1198.
22. Li, S.; Li, L.; Liu, Z.; Wang, G. Microstructure and Its Influence on the Welding Quality of 6063 Aluminum Alloy Porthole Die Extrusion. *Materials* **2021**, *14*, 6584.
23. Yang, Y.; Zhang, Z.; Li, X.; Wang, Q.; Zhang, Y. The effects of grain size on the hot deformation and processing map for 7075 aluminum alloy. *Mater. Design.* **2013**, *51*, 592–597.
24. Cheng, T.C.; Lee, R.S. The influence of grain size and strain rate effects on formability of aluminium alloy sheet at high-speed forming. *J. Mater. Process. Technol.* **2018**, *253*, 134–159.
25. Chrominski, W.; Kulczyk, M.; Lewandowska, M.; Kurzydlowski, K.J. Precipitation strengthening of ultrafine-grained Al–Mg–Si alloy processed by hydrostatic extrusion. *Mater. Sci. Eng. A* **2014**, *609*, 80–87.
26. Chrominski, W.; Lewandowska, M. Precipitation phenomena in ultrafine grained Al–Mg–Si alloy with heterogeneous microstructure. *Acta Mater.* **2016**, *103*, 547–557.
27. Quispe, A.; Medina, S.F.; Gómez, M.; Chaves, J.I. Influence of austenite grain size on recrystallisation–precipitation interaction in a V-microalloyed steel. *Mater. Sci. Eng. A* **2007**, *447*, 11–18.
28. Marioara, C.D.; Andersen, S.J.; Jansen, J.; Zandbergen, H.W. The influence of temperature and storage time at RT on nucleation of the β″ phase in a 6082 Al–Mg–Si alloy. *Acta Mater.* **2003**, *51*, 789–796. [CrossRef]

29. Pogatscher, S.; Antrekowitsch, H.; Leitner, H.; Ebner, T.; Uggowitzer, P.J. Mechanisms controlling the artificial aging of Al–Mg–Si Alloys. *Acta Mater.* **2011**, *59*, 3352–3363.

30. Werinos, M.; Antrekowitsch, H.; Ebner, T.; Prillhofer, R.; Uggowitzer, P.J.; Pogatscher, S. Hardening of Al–Mg–Si alloys: Effect of trace elements and prolonged natural aging. *Mater. Des.* **2016**, *107*, 257–268.

31. Li, S.K.; Li, L.X.; He, H.; Liu, Z.W.; Zhang, L. Influence of dynamic recrystallization on microstructure and mechanical properties of welding zone in Al–Mg–Si aluminum profile during porthole die extrusion. *Trans. Nonferrous Met. Soc. China* **2019**, *29*, 1803–1815.

32. Starink, M.J.; Gao, N.; Kamp, N.; Wang, S.C.; Pitcher, P.D.; Sinclair, I. Relations between microstructure, precipitation, age-formability and damage tolerance of Al–Cu–Mg–Li (Mn, Zr, Sc) alloys for age forming. *Mater. Sci. Eng. A* **2006**, *418*, 241–249.

33. Krol, T.; Baither, D.; Nembach, E. Softening of the superalloy NIMONIC PE16 by precipitate free zones along grain boundaries. *Mater. Sci. Eng. A* **2004**, *387–389*, 214–217.

34. Munitz, A.; Meshi, L.; Kaufman, M.J. Heat treatments' effects on the microstructure and mechanical properties of an equiatomic Al-Cr-Fe-Mn-Ni high entropy alloy. *Mater. Sci. Eng. A* **2017**, *689*, 384–394.

35. Munitz, A.; Kaufman, M.J.; Nahmany, M.; Derimow, N.; Abbaschian, R. Microstructure and mechanical properties of heat treated Al1.25CoCrCuFeNi high entropy alloys. *Mater. Sci. Eng. A* **2018**, *714*, 146–159.

36. Munitz, A.; Cotler, C.; Talianker, M. Aging impact on mechanical properties and microstructure of Al-6063. *J. Mater. Sci.* **2000**, *35*, 2529–2538. [CrossRef]

37. Cuniberti, A.; Tolley, A.; Riglos, M.V.C.; Giovachini, R. Influence of natural aging on the precipitation hardening of an AlMgSi alloy. *Mater. Sci. Eng. A* **2010**, *527*, 5307–5311.

38. Jiang, B.; Cao, F.; Wang, H.; Yi, D.; Jiang, Y.; Shen, F.; Wang, B.; Liu, H. Effect of aging time on the microstructure evolution and mechanical property in an Al-Cu-Li alloy sheet. *Mater. Sci. Eng. A* **2019**, *740–741*, 157–164.

39. He, J.H.; Jin, L.; Wang, F.H.; Dong, S.; Dong, J. Mechanical properties of Mg-8Gd-3Y-0.5Zr alloy with bimodal grain size distributions. *J. Alloys Compd.* **2017**, *5*, 423–429. [CrossRef]

40. Thomesen, S.; Hopperstad, O.S.; Myhr, O.R.; Børvik, T. Influence of stress state on plastic flow and ductile fracture of three 6000-series aluminium alloys. *Mater. Sci. Eng. A* **2020**, *783*, 139295.

41. Liu, G.; Scudino, S.; Li, R.; Kühn, U.; Sun, J.; Eckert, J. Coupling effect of primary voids and secondary voids on the ductile fracture of heat-treatable aluminum alloys. *Mech. Mater.* **2011**, *43*, 556–566. [CrossRef]

42. Frodal, B.H.; Dæhli, L.E.B.; Børvik, T.; Hopperstad, O.S. Modelling and simulation of ductile failure in textured aluminium alloys subjected to compression-tension loading. *Int. J. Plasticity* **2019**, *118*, 36–69. [CrossRef]

43. Fallah, V.; Korinek, A.; Ofori-Opoku, N.; Raeisinia, B.; Gallerneault, M.; Provatas, N.; Esmaeili, S. Atomic-scale pathway of early-stage precipitation in Al–Mg–Si alloys. *Acta Mater.* **2015**, *82*, 457–467. [CrossRef]

44. Zhu, S.; Shih, H.C.; Cui, X.; Yu, C.Y.; Ringer, S.P. Design of solute clustering during thermomechanical processing of AA6016 Al–Mg–Si alloy. *Acta Mater.* **2021**, *203*, 116455. [CrossRef]